



Final Draft of the original manuscript

Bouali, A.; Iuzviuk, M.; Serdechnova, M.; Yasakau, K.; Drozdenko, D.; Lutz, A.; Fekete, K.; Dovzhenko, G.; Wieland, F.; Terry, H.; Ferreira, M.; Zobkalo, I.; Zheludkevich, M.:

Mechanism of LDH Direct Growth on Aluminum Alloy Surface: A Kinetic and Morphological Approach.

In: The Journal of Physical Chemistry C. Vol. 125 (2021) 21, 11687 – 11701.

First published online by ACS: 19.05.2021

<https://dx.doi.org/10.1021/acs.jpcc.1c02281>

Mechanism of LDH Direct Growth on Aluminium Alloy Surface: A Kinetic and Morphological Approach

A.C. Bouali^{1*}, M.H. Iuzviuk², M. Serdechnova¹, K.A. Yasakau³, D. Drozdenko⁴, A. Lutz⁵, K. Fekete⁴, G. Dovzhenko⁶, D.C.F. Wieland⁷, H. Terryn⁵, M.G.S. Ferreira³, I.A. Zobkalo², M.L. Zheludkevich^{1, 8}.

¹ Institute of Surface Science, Helmholtz-Zentrum Geesthacht, Max-Planck-Straße 1, 21502 Geesthacht, Germany.

² Petersburg Nuclear Physics Institute, Laboratory of Physics of Crystals, 188300 Leningradskaya Oblast, Gatchina, 1, mkr. Orlova roshcha, Russia.

³ CICECO - Aveiro institute of materials, Dep. Materials and Ceramic Engineering, University of Aveiro, 3810-193 Aveiro, Portugal.

⁴ Faculty of Mathematics and Physics, Department of Physics of Materials, Charles University, Ke Karlovu 5, 12116 Prague 2, Czech Republic.

⁵ Research Group Electrochemical and Surface Engineering, Vrije Universiteit Brussel, Pleinlaan 2, Etterbeek, 1050 Brussels, Belgium.

⁶ Institute of Materials Physics, Helmholtz-Zentrum Geesthacht, Max-Planck-Straße 1, 21502 Geesthacht, Germany.

⁷ Institute of Metallic Biomaterials, Helmholtz-Zentrum Geesthacht, Max Planck Straße 1, 21502 Geesthacht, Germany.

⁸ Faculty of Engineering, Kiel University, Kaiserstraße 2, 24143 Kiel, Germany.

* Corresponding author: A.C. Bouali, email: anissa.bouali@hzg.de

Abstract

The growth of ZnAl layered double hydroxide (LDH) on the AA2024 surface was monitored using synchrotron high-resolution X-ray diffraction. Kinetic data were extracted and analysed using the Avrami Erofe'ev kinetic model. Accordingly, the LDH film growth is governed by a 2D diffusion-controlled reaction with a zero-nucleation rate. Additional methods including *ex-situ* AFM/SKPFM supported by *in-situ* OCP measurements together with SEM and TEM/EDX analysis, provided further insight into the different stages of the mechanism of LDH growth. Prior to the conversion coating formation, an intermediate layer is formed as a basis for the establishment of the LDH flakes. Moreover, a Cu-rich layer was revealed, which could contribute to the acceleration of LDH growth. The formed LDH layer does not show any cracks

at the interface, but presents minor irregularities in the structure which could favour adhesion to subsequent organic coatings. The findings presented in this work provides an important insight to the corrosion performance of the LDH conversion coatings and the pathway to adopt for further optimization.

Keywords: layered double hydroxide, conversion coating, mechanism, growth.

Introduction

For the past decades, chromate-based conversion coatings (CCC) were an industrial benchmark in terms of corrosion protection for many metallic structures, especially for Al alloys¹⁻⁹. The recent ban, due to their detrimental impact on the environment and human health compelled industrials and researchers to seek new alternatives^{2, 9-12}. However, the outstanding corrosion resistance, stability and durability of CCCs in a broad area of application, renders the development of alternatives very challenging.

A number of prospective substitutes to CCC have been recently proposed and studied^{11, 13-18}. A particular focus was accorded to their mechanism of formation¹⁸⁻²³ since it is key in predicting their corrosion protection efficiency¹⁸⁻²³. For instance, former CCC stores Cr (VI) inhibiting anions in the form of a mixed Cr (III)/Cr (VI) oxide layer and upon exposure to a corrosive media, the Cr (VI) are released and act as inhibitors to the corrosion process^{5, 24, 25}. Cerium- based conversion coating formation on Al alloys relies on a precipitation mechanism mainly driven by the local increase of pH over the cathodic sites (e.g., Cu-rich intermetallic (IMC) on AA2024), leading to the formation of a mixed Ce(III)/Ce(IV) oxide layer over the metallic surface²⁶⁻²⁸. Zirconate/titanate-based conversion coatings are another example of coatings, where nucleation and film growth start from the IMCs succeeded by deposition of hydrated metal oxides (ZrO_2/TiO_2) on the Al metal alloy surface. This hydrated oxide (ZrO_2/TiO_2) offers a passive corrosion barrier protection^{18, 29-31}.

Recently, LDH has caught the attention of the corrosion research community and is considered as one of the next generations of active corrosion protection systems^{9, 32-33}. LDH is part of a novel class of the anionic delivery system that has the capacity to store and release anionic corrosion inhibitors upon different triggers (e.g., pH, chlorides, etc.).

Several studies reported the successful use of LDH in the form of pigments³⁴⁻³⁷ or conversion coatings^{7, 38-41} for the corrosion protection of Al alloys. Regarding LDH conversion coatings, Buchheit et al.⁴² were first to demonstrate the concept by immersing an Al alloy plate into an alkaline solution containing Li salts. The authors referred to the resulting coating as a talc film

based on hydrotalcite-like structure. The formation of the talc film begins by destabilization and dissolution of the native Al oxide layer resulting in the appearance of a series of Al aquahydroxo complexes. The additional presence of the reactants Li^+ and CO_3^{2-} , favoured by the $\text{pH} > 10.5$, leads to talc precipitation from the solution^{40, 42}.

Some years later, Tedim et al.³⁹ suggested a novel LDH nanostructured container layer grown directly on AA2024 substrate relying on Zn^{2+} and Al^{3+} as the main cations for the hydroxide layer and nitrate (NO_3^-) as the interlayer anion. This enables further active corrosion protection functionality by an anion-exchange reaction with the corrosion inhibitor vanadate ($\text{V}_2\text{O}_7^{2-}$).

LDH films have shown to possess a number of compelling properties for the corrosion protection of Al alloys but, there is still a lack of understanding of the LDH film growth mechanism. Recently, Y. Wang et al.⁴³ investigated (*in-situ*) the ZnAl LDH film growth by means of an electrochemical quartz crystal microbalance (EQCM). The study reaffirmed some of the previous speculations^{42, 44-45} with respect to the mechanism of LDH growth on Al alloys. However, an important question: what happens at the early stage of the conversion process, - remains unresolved. Despite the authors comprehensive interpretation of the different stages involved in the LDH growth, the presented timeline (after 10 min) is not practical since at this point a complete LDH film has already been established on the surface.

In the current study, the *in-situ* synchrotron high-resolution X-ray diffraction (XRD) has been used to investigate the LDH growth mechanism on the AA2024-T3 substrate from different perspectives. An *ex-situ* atomic force microscopy combined with scanning Kelvin probe force microscopy (AFM/SKPFM) analysis together with the *in-situ* open circuit potential (OCP) measurements, provides important insight on the reactions taking place at the interface. The morphology and structure of the obtained LDH films were closely examined with a scanning and transmission electron microscopy (SEM and TEM, respectively).

Experimental

1. Materials

1.1. Chemicals

For the LDH preparation, the following reagents were used: zinc nitrate hexahydrate ($\text{Zn}(\text{NO}_3)_2 \cdot 6\text{H}_2\text{O}$, >99%, CarlRoth, Germany), ammonium nitrate (NH_4NO_3 , >98.5%, Bernd Kraft, Germany), ammonia solution ($\text{NH}_3 \cdot \text{H}_2\text{O}$, 25%, Merck KGaA, Germany) and deionized (DI) water.

1.2. Substrate

The AA2024-T3 used in the current work has the following nominal composition in wt. % : 90.7-94.7 Al, 3.8-4.9 Cu, 0.5 Fe, 0.1 Cr, 1.2-1.8 Mg, 0.3-0.9 Mn, 0.5 Si, 0.15 Ti, 0.25 Zn and 0.15 balance.

The size of the specimen was 10x10 mm². In addition to the AA2024-T3 (hereafter AA2024), a 99.99 % purity Al substrate was used to carry out a part of the investigation.

2. Methods

2.1. LDH film growth

The general synthesis procedure is similar to previously reported works^{39, 46, 47}. The synthesis relies on a hydrothermal process in a bath containing a mixture of 0.1 M Zn (NO₃)₂ and 0.6 M NH₄NO₃, with a pH adjusted to 6.5 using 1 wt. % ammonia. The temperature was maintained at 95 °C and the immersion time varied according to the investigating method (from 1 to 30 min)

3. Characterization

3.1. Synchrotron high-resolution X-ray diffraction (XRD)

The *in-situ* investigation of LDH film growth on the AA2024 substrate was performed using a customized testing cell (see supporting information **Figure S1a**) comprising the following items:

- a thermo-couple and resistive heating allowing to measure and control the solution temperature;
- an input and output tubing allowing the solution to enter and exit the cell;
- a Kapton window placed directly in front of the substrate permits the penetration of X-rays.

The solution flow (in and out of the cell) was monitored using a pump neMESYS (CETONI GmbH, Korbussen, Germany) (**Figure S1b**).

The described set-up (**Figure S1c**) was installed on the P08 high-resolution diffraction instrument at the synchrotron radiation source beamline facility at PETRA III (DESY, Hamburg, Germany)⁴⁸. A two-dimensional PERKIN Elmer detector with a pixel size of 200 μm² was used. The X-ray energy of 25 KeV^{48, 49} and wavelength of $\lambda = 0.04952$ nm, were used in this study. The incident angle value was $\Theta = 0.12^\circ$. Diffraction patterns were recorded every 0.54 seconds, immediately after flowing the synthesis solution into the cell in a range of 2θ angles from 2° to 19.6° with respect to synchrotron wavelength.

The radial integration of 2D XRD patterns was performed using GSAS II package. In order to refine the crystal structure and the identification of the atom positions the obtained data were analysed using the FullProf software.

3.2. Atomic force microscopy (AFM)

Atomic Force Microscopy (AFM) and Scanning Kelvin probe force microscopy (SKPFM) analyses were performed using Digital Instruments NanoScope III Microscope equipped with Extender™ Electronic Module. The SKPFM was operated in the interleaved mode with two pass scans. The first scan acquired surface topography. During the second scan, the Volta potential difference (VPD) between the alloy surface and the AFM tip was measured using the nulling technique. The lift-off distance was set to 100 nm and a 5 V RMS AC voltage was induced between the tip and the sample⁵⁰⁻⁵³.

All measurements were done using n-doped silicon probes covered with Pt-Cr layers acquired from Budget sensors. AFM/SKPFM maps with a size of 40 × 40 μm (256 × 256 points) were acquired. Normally, at least two different areas on each sample were analysed in order to reach confident reproducibility. The reported VPD values were obtained as an average from different SKPFM maps with the assistance of the freeware program Gwyddion v2.47. Room conditions during the measurements had a relative humidity (RH) of about 50-55 % and temperature of 22 ± 2 °C. A polished pure Ni surface was used as a reference standard material and the reported VPD values were referenced to Ni. A reference measurement was taken before and after each map.

3.3. Open Circuit Potential (OCP)

OCP measurements were carried out using an Interface 1000E potentiostat/galvanostat/ZRA (Gamry, USA) monitored with a Gamry framework system. A silver/silver chloride (Ag/AgCl) electrode was employed as a reference electrode. Two OCP measurements were carried out:

- 1) AA2024 substrate immersed in a solution with the suitable conditions and precursors for LDH growth.
- 2) AA2024 immersed in DI water.

In both cases, the temperature was maintained at 95 °C and the solution was continuously stirred. The recording of the OCP data started as soon as the AA2024 sample was immersed into the solution.

3.4. Scanning electron microscopy (SEM)

SEM micrographs representing the top view of the samples surface during LDH formation were taken using a Tescan Lyra 3 set-up (TESCAN GmbH, Dortmund, Germany). The data was analysed with the Aztec software supplied by the Oxford Instruments.

For analysis of the cross-section of the LDH coatings, a thin lamella was extracted using a focused ion beam (FIB) of Ga⁺ ions in Zeiss Auriga Compact Cross Beam SEM (Zeiss, Germany). The surface of the LDH layer was preserved by Pt covering before the FIB sectioning. The lamella was mounted on the Cu grid. Prior to TEM analysis, secondary electrons (SE) images of the cross-section view of the LDH coatings were obtained by SEM.

3.5. Transmission electron microscopy (TEM)

The microstructure and chemical distribution of the cross-section of LDH coatings were investigated using TEM (JEOL JEM-2200FS, JEOL Ltd., Japan) operating at 200 kV equipped with the EDX system.

Results

1. Analysis of the crystal structure and kinetics

The XRD patterns recorded during LDH formation were collected and plotted as a function of time in **Figure 1**. **Figure 1a** represents the evolution of the patterns over a timescale of 100s with a 2θ range of 2-12°, whereas **Figure 1b** shows the same patterns with a reduced timescale of 30 s and a 2θ range of 2-7°.

As illustrated in **Figure 1b**, the emergence of the first crystal phases associated with LDH appears approximately at 21.6 s after the start of the conversion reaction. This was identified by the appearance of the (003) reflection at 3.182(5)°. The (006) reflection at 6.361(6)° appears much later. The intensity of the basal reflections is dependent on the metal cations (Al, Zn) scattering in the host layers and the guest anion (NO₃⁻) do not possess a high scattering power. This implicates a decrease of the (006)/ (003) reflection ratio as *t* increases, which explains the late manifestation of the (006) reflection³³.

In addition to the LDH phases, two relevant secondary phases corresponding to the Al₂CuMg and Al₇Cu₂Fe IMCs were identified. From **Figure 1**, one can notice that the intensity of the XRD peaks associated with a few IMCs decreases over time. For instance, the intensity of the (002) reflection ascribed to the Al₇Cu₂Fe IMC (indicated with an arrow in **Figure 1**) continuously decreases with time. There are two possible hypotheses to explain this

observation; the first explanation is a possible partial dissolution of the IMC phases, which affects the signal from the IMCs due to a loss of the scattering centres from the corresponding crystalline phase. The second hypothesis is that the LDH layer progressively covers the surface of the AA2024, including the IMC sites, hence less signal can be acquired from this area of the interface. A noticeable amorphous halo can also be observed in the patterns, which may be attributed to the signal from water.

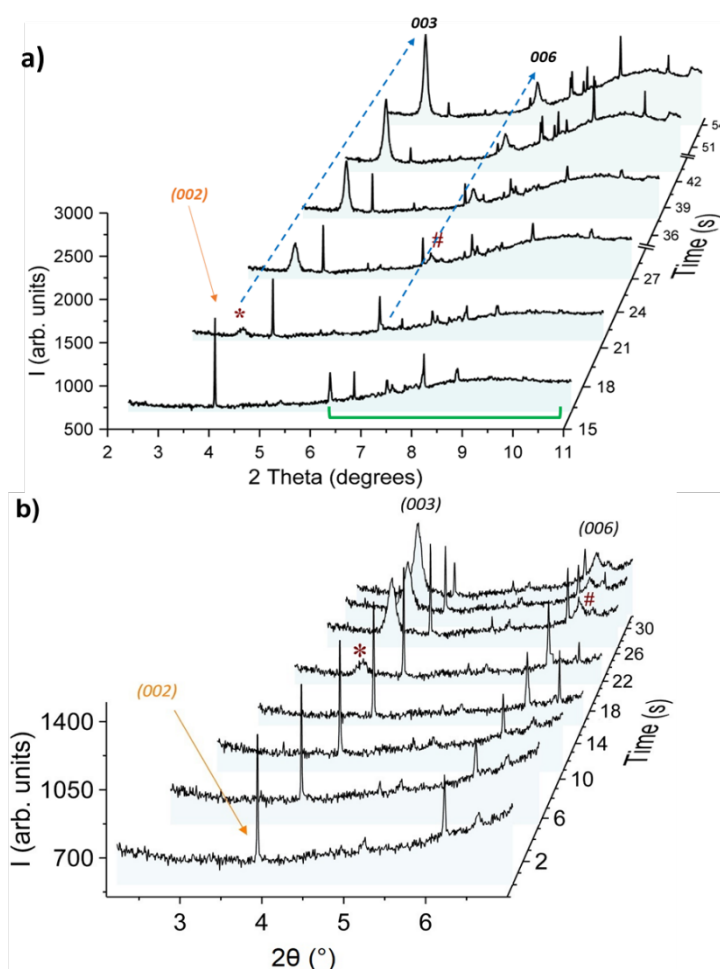


Figure 1. Time series of XRD patterns for the LDH-NO₃ growth on AA2024 during the entire measurement period of 100 s **a)** and enlarged view of the first 30 s with a reduced 2θ range and rescaled intensity **b)**. (003) and (006) peaks are marked by * and #, respectively. The green parenthesis indicates the amorphous halo.

The crystal structure of LDH was refined, using as a basis, the rhombohedral space group R-3m (see supporting information **Figure S2**). A table listing the observed reflections associated with LDH and the AA2024 substrate is represented in **Table S1** (supporting information).

The ZnAl LDH-NO₃ unit cell parameters and atomic coordinates are given in **Table 1**. From the table, one can conclude that the NO₃⁻ atomic position is of type 36i and the angle between

the hydroxide layer and the NO_3^- plane is about 70° as previously deduced in other studies^{49, 54}.

Using the information presented in **Table 1**, the asymmetric unit cell corresponding to the ZnAl LDH- NO_3 was built using the VESTA software (**Figure 2a** and **b**). The whole unit cell is constructed using the symmetry operations of R-3m space group. **Figure 2a** shows a rhombohedral unit cell with the distribution of the individual atoms from the different groups involved in the LDH structure.

Table 1. ZnAl LDH- NO_3 unit cell parameters and atomic coordinates

Unit cell parameters				
a		3.076(2) Å		
c		26.688(3) Å		
R _p		5.34		
χ^2		2.44		
Atomic coordinates				
Atom	Position	x	y	z
Zn/Al	3a	0	0	0
O _h	6c	0	0	0.370(2)
N	36i	0.49(6)	0.86(3)	0.160(7)
O ₁	36i	0.30(3)	0.90(2)	0.152(2)
O ₂	36i	0.63(5)	0.81(3)	0.140(2)
O ₃	36i	0.49(3)	0.961(2)	0.210(2)
O _w	18h	0.12(1)	-0.12(1)	0.886(1)

The atoms O₁, O₂ and O₃, which are part of the NO_3^- anions are not shared with the other groups. The O_w is one oxygen atom from the water molecules situated in the LDH galleries. Removing the NO_3^- anion from the model of the unit cell (**Figure 2b**) allows better visualization of the other atoms, e.g., the position of the other oxygen atoms.

The Al and Zn atoms are indicated in **Figure 2b** by the small grey spheres. It was assumed that the cations are randomly distributed in position 3a and the designation "Zn/Al" shows that in these particular positions, it is unknown which cation predominates. The rhombohedral structure, shown in **Figure 2a** and **b**, is regarded as the hexagon structure unit (**Figure 2c**). This

latter is attached to a chain of hexagons that constitutes the actual LDH framework. The atom O_h together with the shared Zn/Al form part of the hydroxide layers composing the building blocks of LDH.

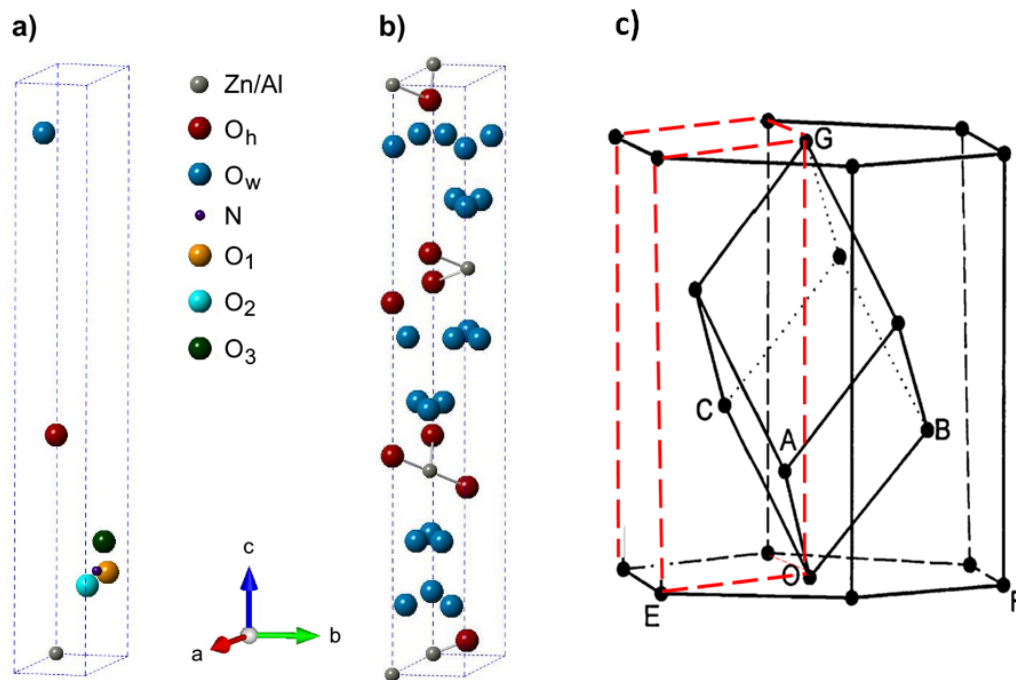


Figure 2. Asymmetric unit cell of LDH-NO₃ built using coordinates from Rietveld refinement representing the positioning of all main atoms with NO₃⁻ **a)** and the whole cell without the NO₃⁻ **b)** allowing a better focus on the other compositions, and a representation of the rhombohedral unit cell implemented on a hexagone **c)**. Reprinted in part with permission from (33) Evans, D.G.; Slade, R.C.T. In Layered Double Hydroxides. Structure and Bonding; Duan, X., Evans, D.G., Eds.; Springer: Berlin, Heidelberg, 2006, Vol. 119, pp 1-87. Copyright 2006 Springer.

2. Ex-situ AFM/SKPFM measurement

The AFM/SKPFM measurements will provide insight into the changes happening at the interface, from both a surface topography perspective, but also the Volta potential changes overtime. The tests were performed in an *ex-situ* manner with respect to immersion time (from 60 to 900 seconds).

Figure 3a presents the selected topography and VPD maps of the AA2024 surface before and after different immersion times in the LDH synthesis bath. The topography map before immersion (at 0 s) shows a polished metallic surface that does not unambiguously pinpoint the location of the IMCs on the surface (**Figure 3a** “0 s”). On the opposite, the VPD map (**Figure 3a** “0 s”) shows scattered IMCs, dispersoids and small constituents which normally display a brighter contrast, more positive potential vs. the Al matrix, on the Volta potential maps^{55, 56}.

After immersion for 60 s (**Figure 3a “60 s”**), the first visible changes appeared on the topography map, which are caused by the growth of an LDH conversion layer on the surface. The IMCs and scratches observed before immersion were no longer visible, and the map displays a noticeable contrast with the matrix which shows a type of round shaped zones (**Figure 3a “60 s”**).

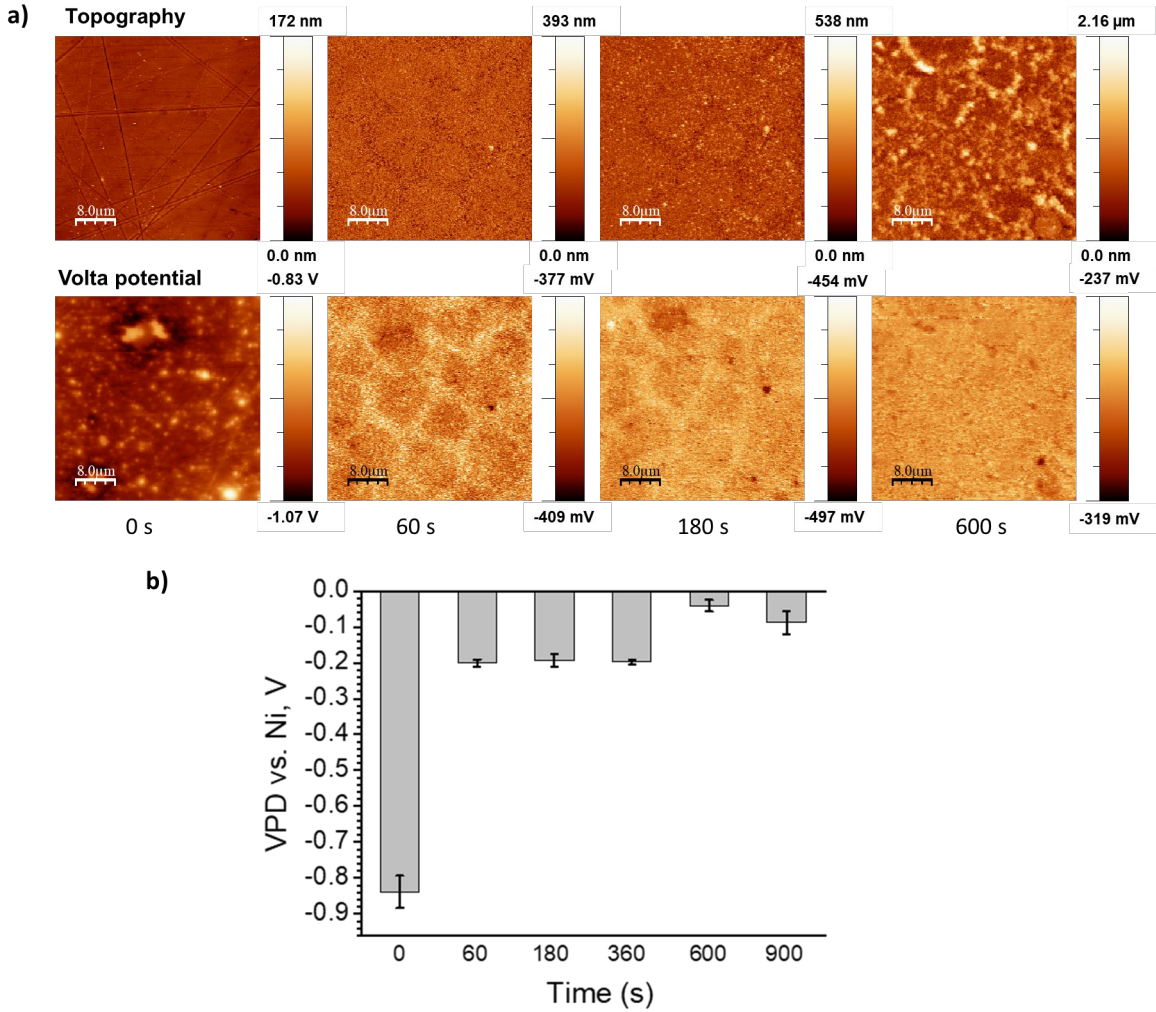


Figure 3. Images of the topography (top) and VPD maps (bottom) of the AA2024 surface **a)** and the values of VPD changes **b)** before and after different immersion times in the LDH synthesis bath.

These latter zones could be associated with the AA2024 grains. It appears that at the early stage of immersion, the LDH covers preferentially the grains interior but not the grain boundaries. This preferential nucleation on grains was reported previously for CCC formation on Al alloys^{57,58}. However, there is overtime bridging of the conversion coating across the grain boundaries, allowing full coverage of the entire sample surface⁵⁷.

The LDH conversion layer grows with time, and the height profile of the topography increases from 60 to 600 s of immersion (**Figure 3a**). However, VPD maps show much less contrast with increasing immersion time (**Figure 3a**).

Apart from the lack of contrast on the VPD maps, the average VPD levels measured on the surface increases, as it can be seen from the diagram in **Figure 3b**. This becomes obvious even after 60 s immersion in the LDH synthesis bath, where an increase to more positive VPD values (-0.2 V vs. Ni) in comparison to that in the initial state (about -0.84 V vs. Ni) was observed (**Figure 3b**). There was an increase of VPD values until about -0.05 V and -0.08 V vs. Ni after immersion up to 600 and 900 s, respectively. It is known that changes in the composition of the passive film⁵⁹, the presence of anodic oxide films on Al surface⁶⁰ and the distribution of Cu on the surface of AA2024⁶¹ may contribute to the measured Volta potential. For instance, the VPD potential of polished pure Cu is about 0 V vs. Ni. The VPD measured on the alloy after 600-900 s of immersion is just slightly lower than that of pure Cu (**Figure 3b**). Such values of VPD are most likely attributed to the distribution of Cu at the interface bordering the Al matrix, though the properties of the conversion layer can also contribute to VPD values.

To better understand the contribution of different factors to the measured VPD values, an additional comparative experiment was designed, by immersion both AA2024 and pure Al (99.99 %) samples in DI water at 95°C instead of the LDH synthesis bath. The results are presented in the supporting information (**Figure S3** and **Figure S4**)

The AA2024 surface before immersion (**Figure S3** “0 s”) displays the same features as (**Figure 3a** “0 s”). After immersion in DI water, the dispersoids and inclusions undergo partial dealloying/dissolution forming small pits that are visible on the topography maps (**Figure S3** “360 s”). Volta potential maps reveal that the small inclusions with higher VPD values (brighter colour) in comparison to the matrix before immersion, become darker after immersion (**Figure S3**). A plausible explanation for that may be the dissolution of the inclusions and the redeposition of more noble elements (e.g., Cu). Cu oxide has also been reported to exist on the surface of Cu-containing alloys before and after corrosion in neutral electrolytes^{62, 63}.

The measured VPD values are a bit different than the ones obtained in **Figure 3b**, but they follow a similar trend (**Figure S3**). After 360 and 900 s of immersion, the average VPD level increased to approx. -0.44 and -0.60 V, respectively, which are more positive compared to the initial level (approx. -0.87 V vs. Ni) (**Figure S4**). It probably takes more time to complete the dealloying and redeposition of Cu on the surface.

When a pure Al was immersed in DI water at 95 °C, VPD decreased to more negative values (-1.38 V vs. Ni) compared to the initial state (“0 s”, -1.22 V vs. Ni) (**Figure S3**). The VPD values for pure Al after immersion are roughly the same as those presented in the earlier work ca. -1.33 V⁶⁰. While a pure Al oxide/hydroxide film does not provide a significant contribution to VPD values, the Cu redeposition process is most likely responsible for the changes of VPD on the AA2024 surface. Cu-dealloying has been previously reported in DI water⁶⁴, which may be the mechanism behind the Cu-redeposition. In order to support this hypothesis, an additional set of electrochemical and microstructural experimental results are presented in the next sections.

3. Open circuit potential measurements and associated SEM images

To support the results obtained by AFM/SKPFM, OCP measurements were performed on the AA2024 samples immersed in DI water (95°C) or subjected to LDH growth (Hydrothermal) bath. The results are shown in **Figure 4**.

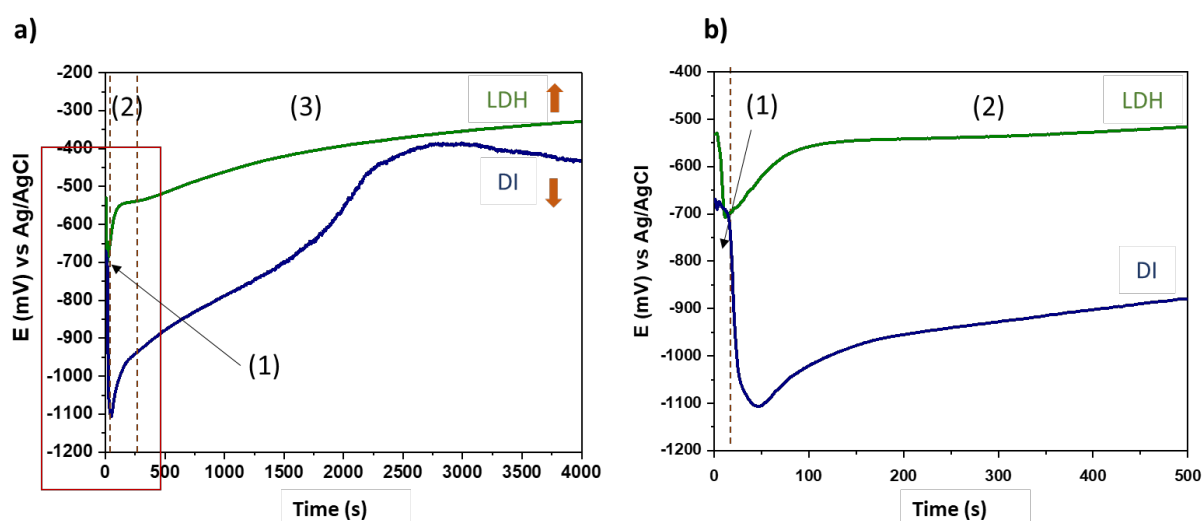


Figure 4. OCP measurements of the AA2024 subjected to the LDH synthesis bath (curve in green) and DI water (curve in blue) for 4000 s **a)** and **b)** enlarged view of the area of the curves between 0 and 500 s.

From the OCP results, three main stages of the LDH formation (**Figure 4a** “green curve”) can be distinguished. At the first stage (approx. 0-12 s), an immediate decrease of the OCP from -530 mV_(Ag/AgCl) to -710 mV_(Ag/AgCl) is observed with the first contact of the AA2024 substrate with the Zn(NO₃)₂ solution (**Figure 4b**). This decrease of the potential can be associated with the depassivation and dissolution of the native Al₂O₃ oxide layer⁴³. According to the *in-situ* XRD measurements (**Figure 1**), no LDH formation occurs at this stage (< 12s). This means that the native oxide layer dissolution reaction takes place first, followed by the first LDH flakes

nucleation. The second stage (approx. 12-260 s) is characterized by an increase of the OCP till it reaches the first plateau at around $-540 \text{ mV}_{(\text{Ag}/\text{AgCl})}$.

The increase of the potential happens around the time where the first LDH flakes formation was observed. Indeed, the first LDH reflection emerged at around 21.6 seconds (**Figure 1**).

Finally, at the third stage ($> 260 \text{ s}$), a continuous increase of the OCP is observed until it reaches certain stability. This region of the OCP portrays an ongoing LDH film growth and crystallization. The results demonstrated by the current OCP measurement are in agreement with the SKPFM measurements (**Figure 3**) as well as with the literature^{43,45}. While the OCP increases with the increase of the LDH growth, the OCP of the AA2024 sample in DI water increases till a peak at approx. -382 mV ($\sim 3300 \text{ seconds}$) but then start to decrease.

It is worth mentioning that the measurements include a slight margin of error (1-2 s) from the start of the OCP recording. However, the experiment was repeated at least three times to ensure reproducibility.

Further *ex-situ* observations were done by taking SEM images on the AA2024 surface in order to monitor the changes through the different stages of the LDH nucleation and film growth. **Figure 5a** shows the AA2024 surface before immersion. After 30 s of immersion (**Figure 5b**), a uniform flake-like LDH film can already be seen at the interface of the AA2024 substrate. This is in agreement with the detection of the first XRD peaks associated with LDH at 21.6 s (**Figure 1**).

Figure 5b, c and d display the evolution of the LDH layer after immersion for 30 s, 60 s, and 180 s, respectively, belonging to the second stage of the LDH film formation. At this stage, the ongoing formation of the LDH flakes seems to progressively fill the voids (the areas that were free of LDH) left at the AA2024 surface. After 360 s, which supposedly marks the 3rd stage of the LDH growth, a continuous evolution of the LDH growth takes place (**Figure 5e, f and g**). The LDH film looks more compact and denser than it was at the 2nd stage of formation. This change has been noticed with the SKPFM measurements, where a further increase of the potential was detected. The SEM images (**Figure 5a-f**) clearly justify the obtained OCP results (**Figure 5h**) and support the assumption that there are different stages to the LDH formation mechanism.

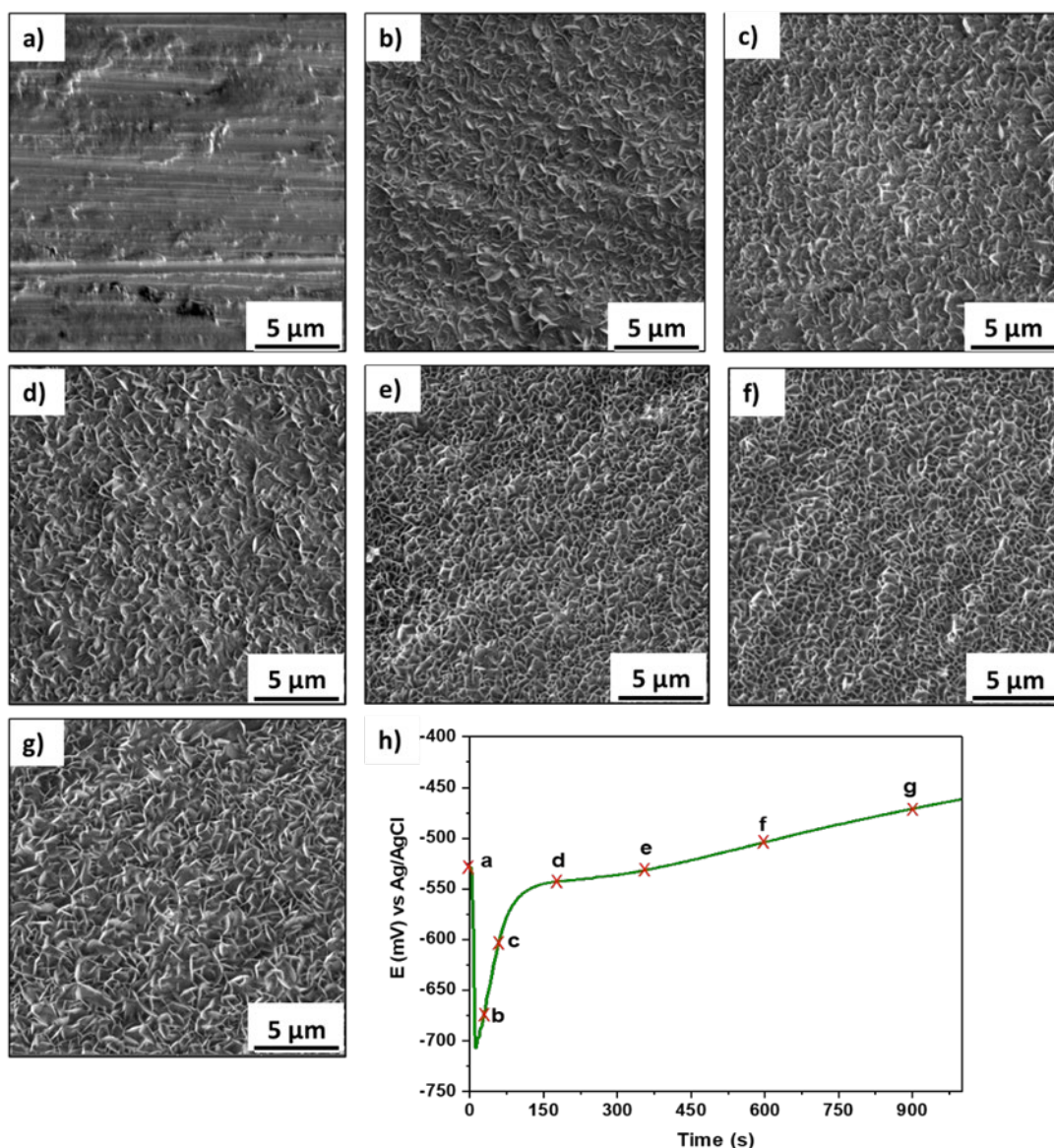


Figure 5. SEM images of the AA2024 sample before immersion **a)** and after immersion for 30 s **b)**, 60 s **c)**, 180 s **d)**, 360 s **e)**, 600 s **f)**, 900 s **g)** in the LDH synthesis bath, and their positioning in the OCP curve representing the LDH growth over time **h)**.

4. Cross-section view of LDH conversion layer grown on the AA2024 substrate: TEM analysis

Since the top-view SEM images do not allow a closer and direct look into the LDH flakes at the AA2024 interface, lamella representing a cross-section of the AA2024 substrate coated with ZnAl LDH conversion layer was prepared and analysed using TEM (**Figure 6**). It is important to mention that the AA2024 substrate has been immersed for 30 min in the synthesis bath to make sure that the LDH conversion layer reaches the right maturity and thickness to obtain good TEM images.

Figure 6b-d depict a configuration of organized flakes that are overall rather perpendicular to the AA2024 interface, except for the few regions where an accumulation of different oriented LDH flakes can be observed.

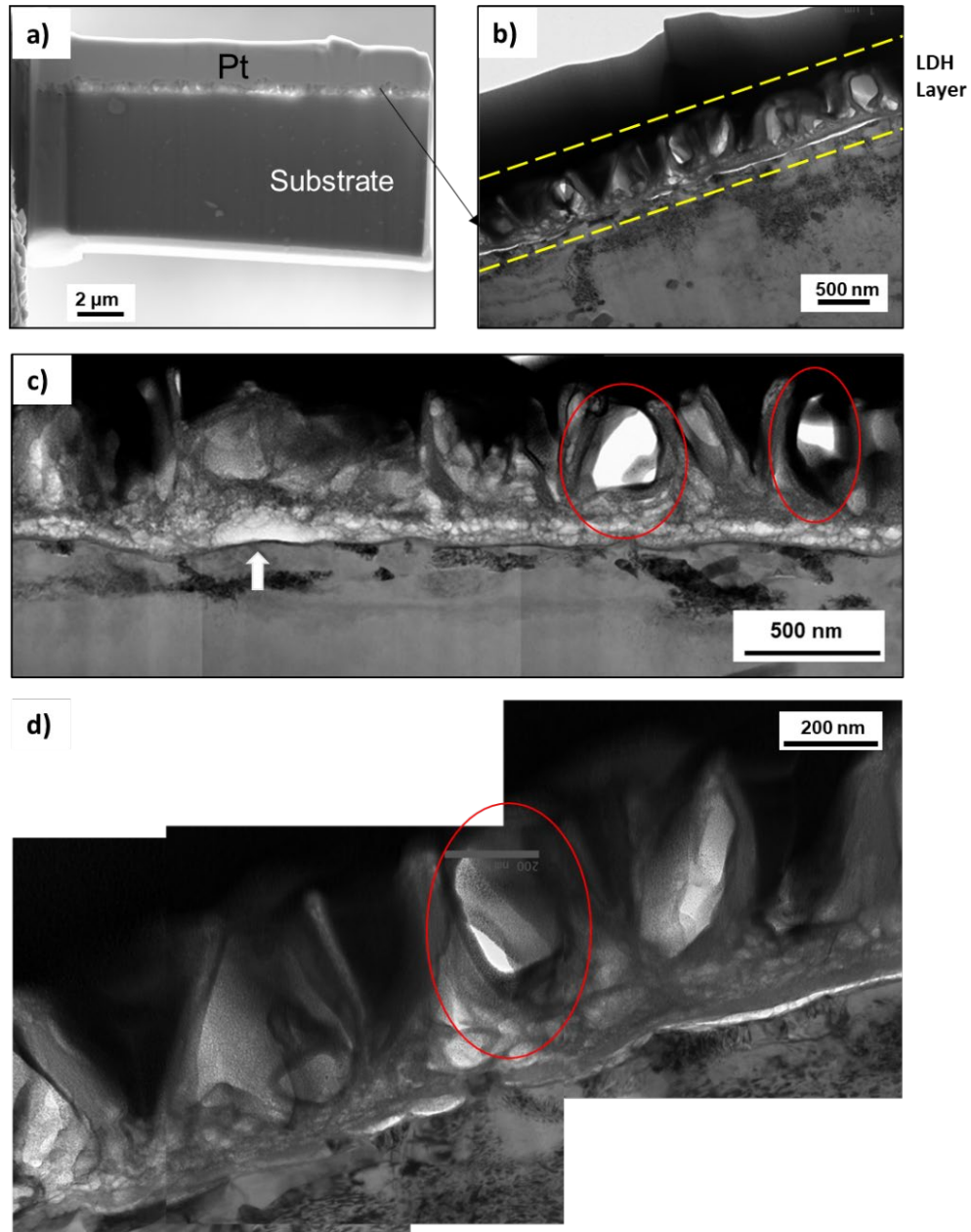


Figure 6. Cross-section images of ZnAl LDH conversion layer grown on AA2024 sample observed by SEM **a)** and TEM (STEM mode) **b), c)** and **d).**

These perpendicular flakes are not built too close to each other, and a certain void can be observed between the flakes (circled in red **Figure 6c** and **d**). However, there are no cracks or disbonding at the interface between the substrate and the LDH layer.

An intermediate layer along the AA2024 interface below the LDH flakes is observed, **Figure 6c** and **d**. This additional layer (~50 nm in thickness) is most probably formed at the initiation step before the growth of the first LDH flakes.

The cross-section region (on the right side of **Figure 6c**) was subjected to an EDX analysis. From the EDX maps (**Figure 7**), the intermediate layer seems to be mainly composed of Al, Zn, O and N, which are also the main elements of the LDH flakes.

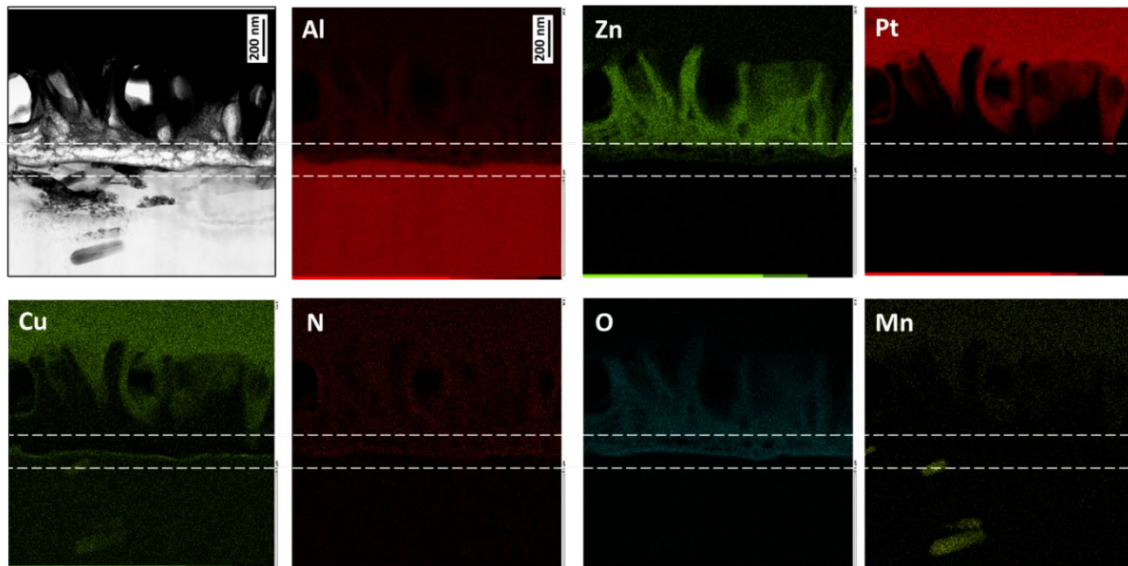


Figure 7. EDX maps for the cross-section of the LDH conversion layer.

A few Mn-rich IMC phases are observed in the AA2024 substrate (**Figure 7**). From the Cu map, a strong Cu signal seems to be emitted from the Pt protective layer. This is an artificial effect since during EDX analysis the electron beam interacts with Pt (a heavy element), leading to the emission of a high number of secondary electrons. These electrons scatter on the Cu grid and are subsequently registered as Cu on the detector, while the electron beam is still focused on the protective Pt layer.

Nevertheless, the redeposition of a thin Cu layer directly at the interface of the Al substrate (below the intermediate layer) can be assumed from TEM image (dark film marked by the white arrow in **Figure 6c**). This could be the result of a selective dissolution of Al from the Al-Cu solid solution in the α -matrix grains involving the Cu-redeposition stage, during the LDH nucleation phase.

Besides the maps, further EDX analysis to discern the changes in the elemental distribution along the interface, intermediate layer, and LDH flakes has been performed (**Figure 8**). Both the profile analysis (**Figure 8a**) and the spot analysis (**Figure 8b** and **c**) show that the intermediate layer and LDH flakes are rich in Al, Zn, O, and N.

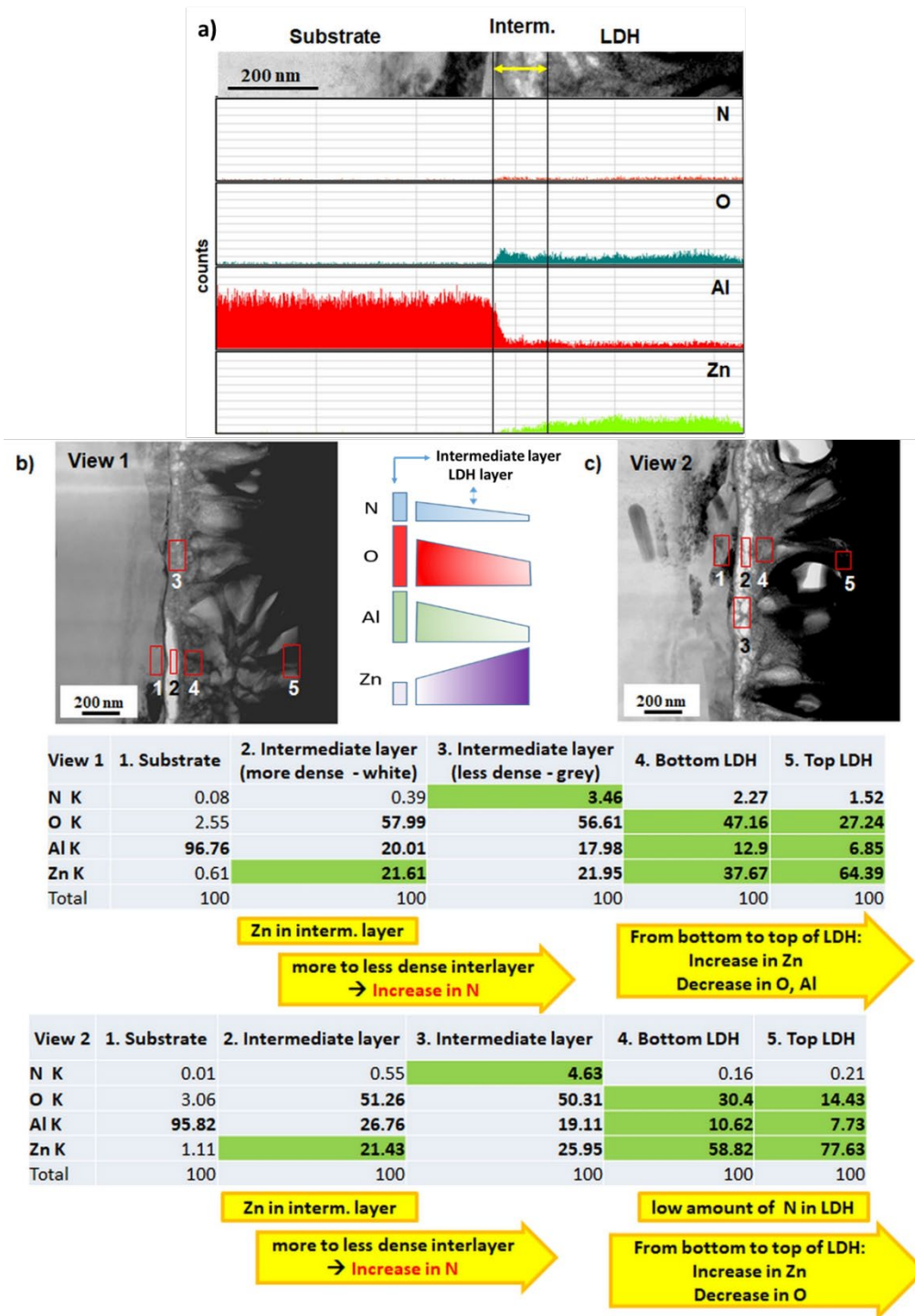


Figure 8. TEM/EDX analysis represented by profile analysis across the LDH conversion layer on the AA2024 substrate (a) and selected areas at different places on the sample (b) and (c). The elemental distribution is expressed in wt. %.

From the spot analysis, the main tendencies of element's distribution from the characteristic regions (marked from 1 to 5 and corresponding to substrate, intermediate layer etc.) are similar for two different places of the cross-section of the LDH coating, view 1 and 2 in **Figure 8b** and

Figure 8c, respectively. The schematic view of elements concentration gradient from intermediate layer toward the top of the LDH layer is depicted between **Figure 8b** and **c**.

For instance, the increase in Zn and decrease in O and Al is observed from bottom to top of LDH layer (region 4 → region 5). At the same time, the intermediate layer is characterized by a higher amount of O comparing to LDH flake region and substrate, which indicates on oxide/hydroxide nature of the intermediate layer. Moreover, the penetration of Zn from LDH layer to the intermediate layer is obvious from profile analysis. Thus, the formation of ZnO products can be expected^{65,66}.

The LDH layer (region 4-5) presented in view 2 has a significantly lower amount of N compared to the one in LDH layer in view 1. However, in both cases (views) higher concentration of N is observed in the intermediate layer (region 3) than that in the LDH layer.

An inhomogeneity of N distribution is also observed along the intermediate layer (region 3 → region 2). When less amount of N penetrates to intermediate layer (region 2), a higher amount of Al and O is observed in the oxide layer resulting in a denser (white) structure.

Discussion

1. Kinetics of LDH growth

The kinetics data from the *in-situ* synchrotron XRD measurements were analysed by the Avrami-Erofe'ev (AE) kinetic model⁶⁷⁻⁷¹. It has been previously applied to investigate the kinetics of LDH anion-exchange reaction^{49,72}. The AE equation can be expressed as following:

$$\alpha(t) = 1 - \exp\{-[k(t - t_0)]^m\} \quad (1)$$

where t_0 [s] represents the induction time of the reaction and k [1/s] is linked to the reaction rate. The extent of the reaction $\alpha(t) = I_{hkl}(t)/I_{hkl}(max)$, where $I_{hkl}(t)$ is the integral intensity of (hkl) peak and $I_{hkl}(max)$ is the maximum intensity of this peak. To obtain a good fit between the equation and the experimental data, the α value should be in the range between 0.15 and 0.85. The other important parameter of the equation is the value of m – index of reaction, which allows disclosing the steps involving the formation of the nucleus and its growth. The time dependence of the integral intensities of (003) peaks was used for kinetics analysis of LDH-NO₃ growth.

The first step of the analysis is a preliminary estimation of the reaction index m by the Sharp-Hancock plotting, which can be derived from the AE equation as following⁷³.

$$\ln(-\ln(1-\alpha)) = m \cdot \ln k + m \cdot \ln(t - t_0) \quad (2)$$

It is based on the assumption according to ⁷⁴, that the AE approach could not be used for an entirely diffusion-controlled reaction, for which $m \sim 0.5$.

From the Sharp-Hancock plot, the m value was found to be approximately 0.90(6) (**Figure 9a**), and this value permits the use of the AE model. Moreover, the least square fitting of a kinetic curve (α vs. t (s)) using the equation (1) gives an m -value of 0.92(6) (**Figure 9b**) with a convergence of $R^2 = 0.98$.

According to the literature ⁷¹, the m -value from the AE equation ($m \sim 0.92$) points either to a one-dimensional diffusion-controlled reaction with a deceleratory nucleation rate or to a two-dimensional reaction with zero nucleation rate.

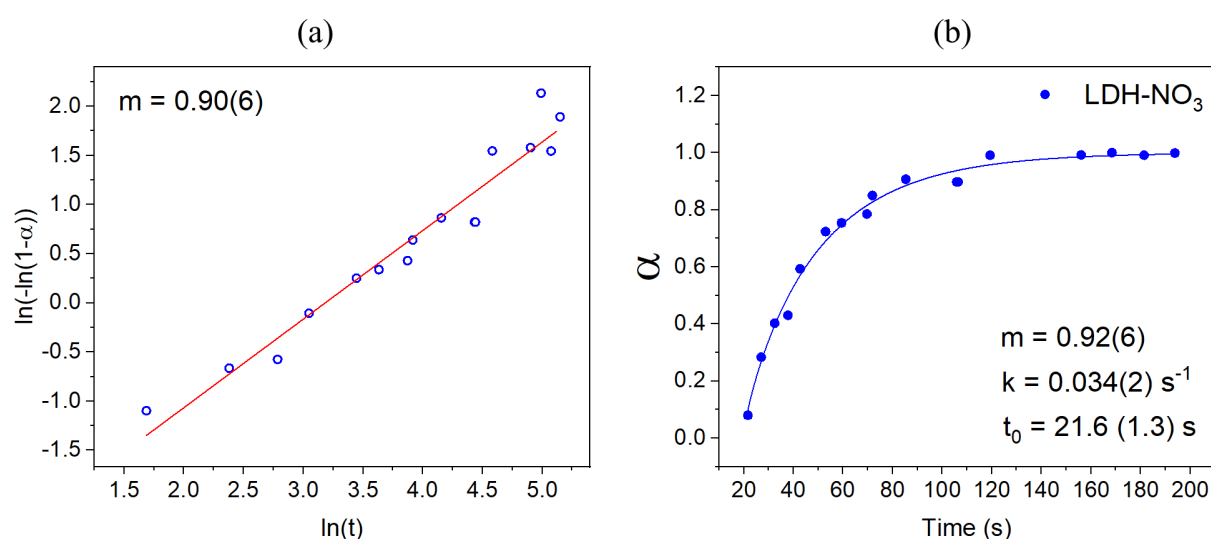


Figure 9. Sharp-Hancock plot for the Zn-LDH-NO₃ growth **a)** and the obtained fitting using the Avrami-Erofe'ev equation **b).**

For layered materials such as LDH, it can be assumed that the growth takes place in two dimensions, equivalent to the movement of the guest anions between the xy -planes of the hydroxide layers. Assuming that in a given ideal lattice there are a number of nucleation sites presumably identical and resulting in the same probability of nucleation, two nucleation reactions are possible. First, as the reaction proceeds the number of nucleation sites decreases (deceleratory nucleation). Deceleratory nucleation involves a slow transportation rate, which could involve the formation of intermediate reaction products. However, the analysis of the patterns obtained at every 0.54 s has not indicated any traces of intermediates formation.

The second possibility is that all the mentioned nucleation sites are saturated instantly as soon as the reaction starts. This is referred as a zero-nucleation rate. This is the more accepted hypothesis.

After the nucleation step, the growth continues following a diffusion controlled-reaction. At this point the growth is not influenced anymore by the nucleation rate but is controlled by the diffusion of the reactant, over the concentration gradient in the solution, to the crystallization sites^{70, 71, 75, 76}.

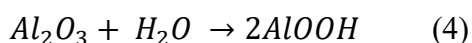
In addition to the above kinetic calculations, the evolution of the LDH flake size “L” was determined using the Scherrer's equation (3)^{72, 77, 78}.

$$L = K\lambda/\beta\cos\theta \quad (3)$$

where K is the Scherrer's parameter (~ 0.9), λ is the wavelength, β is the Full Width at Half Maximum (FWHM) and θ is the Bragg angle. For the analysis, the FWHM of the (003) reflections were considered. The time dependences of FWHM and flake sizes are presented in **Figure S5**. For instance, the maximum value of FWHM at the beginning of the reaction at (21.6 s) is $\beta=0.18(2)^\circ$, which translated to a flake size of $L=14.0(1.6)$ nm. During the LDH formation process, this value became smaller, hence the average flake size increases. Therefore, at the end of the observed period (~ 193 s), FWHM reaches the minimum of $\beta= 0.0620(4)^\circ$ with a flake size of $L= 40.7 (0.3)$ nm. This shows that the thickening of the LDH layer is associated with an increase in the LDH flake size. It is expected that as long as enough reactants are present, the LDH flake size will continuously increase, leading to the formation of a dense and thick LDH layer. This corroborates the TEM images in **Figure 6** and previously reported studies where SEM cross-section images of LDH layers grown on a metal substrate were taken^{79, 80}.

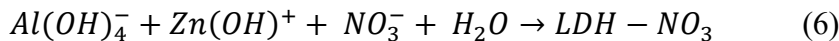
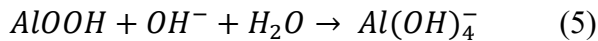
2. Intermediate layer and stages of LDH growth

According to the AFM/SKPFM and OCP results, prior to the appearance of the first LDH flakes, a depassivation of the native oxide layer (Al_2O_3) takes place, followed by its rapid dissolution. It is suggested that the OH^- present at the interface is incorporated into the Al oxide layer leading to the formation of an intermediate layer. Moreover, previous studies on LDH formation reported the formation of an intermediate gel-like $\text{Al}(\text{OH})_3$ layer due to an increase of the local pH prior to the appearance of the LDH flakes^{66, 81}. However, it is also believed that following an increase of the local pH, a cathodic dissolution of the native oxide layer will lead to the generation of an AlOOH pseudo-boehmite layer (equation 4). At the same time, the exposed underlying Al metal may drive further reduction of water to recreate the protective oxide layer. The latter reaction is characterized by the generation of H_2 , which explains the gas evolution (small bubbles) that appear at the substrate's interface during LDH synthesis^{82, 83}.



An amorphous halo was detected on the XRD patterns recorded at the first seconds of the measurements. Earlier in the study, this amorphous halo was associated with a signal from water, but it could also be linked to the emergence of a pseudo-boehmite phase.

Nevertheless, further increase of the local pH destabilizes the formed pseudo-boehmite intermediate layer leading to its partial dissolution and liberation of $Al(OH)_4^-$ (equation 5) ions that will consequently react with $Zn(OH)^+$ to form the LDH flakes (equation 6) ⁸⁴ :



3. Role of Cu in the alloy on the LDH growth

In addition to the above reactions, the AFM/SKPFM results together with the TEM-EDX images, demonstrated evidence of the contribution of Cu in the LDH growth mechanism. Cu-redeposition and thus the formation of a thin Cu layer at the interface may accelerate the dissolution of the Al matrix through a galvanic coupling effect and further generation of OH^- at the interface. Buchheit et al. suggested that following an S-phase dealloying, nanometer size Cu particles (~ 10 nm) can disconnect from the S-phase remnant and lead to their redistribution by dissolution/back-plating ⁸⁵. In the same context, Vukmirovic et al. suggested that Cu redistribution is supported not only by a dissolution/back plating mechanism but also by a matrix dealloying ⁸⁶.

More recently, A. Kosari et al. conducted another detailed investigation of the mechanism of local dealloying of AA2024 ^{87,88}. It has been shown that following the dealloying process of S-phase (Al_2CuMg) and θ -phase (Al_2Cu), some segments of these IMCs may detach and acquire their own free-corrosion potential. Subsequently, the segments will undergo an anodic dissolution process and liberate Cu ions that can be redeposited on the same corroding area or on other active Cu-rich regions⁸⁷. The process is supposed to be similar in both S-phase and θ -phase. However, there are some differences in the amount of liberated Cu ions and their redistribution. For instance, in the case of the corroding θ -phase, it will be covered by $Al(OH)_3$ gel and will progressively become a Cu oxide remnant after its detachment. However, it could still release Cu ions from the lower detached area of the particle. On the other hand, S-phase compounds induce a larger Cu redistribution since Cu is liberated from various sides of the

compound. An important amount of released Cu from S-phase could potentially result on a Cu-replating on the Al matrix⁸⁷.

Moreover, IMCs were not the only source of Cu redistribution since other Cu-rich particles such as dispersoids as well as the matrix (with approx. 0.5 wt. % of Cu in solid solution) could also contribute, but over a different time-scale^{87, 88}. Nevertheless, the deposited Cu clusters induced further dissolution of the Al matrix through a nano-galvanic coupling effect, which leads to a continuation of the events by further detachment of the clusters followed by redeposition and dissolution⁸⁷.

Apart from the anodic dissolution of the Al matrix around the IMC regions, contributions of other alloying elements were not observed. For instance, a possible formation of MgAl LDH around the S-phase as a result of a selective dissolution⁸⁷⁻⁸⁹ and release of Mg^{2+} , was not identified in the current study.

At the same time, essential hypothesis regarding the possibility of a Cu complexation reaction should be underlined. The presence of aqueous ammonia in the LDH synthesis bath could exert an important action on the Cu particles present on the AA2024 surface⁹⁰⁻⁹⁴. It has been shown that ammonia can favour Cu dissolution in the presence of oxygen. Moreover, nitrates resulting from the precursors could further enhance the dissolution process of Cu due to its oxidizing power⁹⁵. Presumably the dissolution of Cu particles on the AA2024 in the presence of ammonia, takes place through the cathodic reduction of oxygen at the Cu surface that is simultaneously followed by the anodic dissolution of Cu and reaction with NH_3 , hence forming various forms of Cu complexes⁹⁰. This could explain the enrichment of N at the intermediate layer in **Figure 8**.

Cu-redistribution as a result of a dealloying effect or a complexation reaction can take place at the same time, one does not systematically exclude the other. Given the complexity of the environment and the lack of data, it is challenging to establish which process is predominant.

The key function of Cu-rich particles during conversion coating formation has been reported previously^{18, 96-98}. For instance, Cu-rich IMC was shown to induce the co-precipitation reaction such as precipitation of hydrated zirconia/ $Cr(OH)_3$ in the formation of trivalent chromate conversion coating⁹⁶ and the precipitation of the Zr/Ti metal oxide for the formation of the respective Zr/Ti conversion coating¹⁸. Regarding LDH conversion coating formation, a few

studies highlighted the presence of LDH islands on Cu-rich IMC areas^{49,39}. This was associated with an acceleration of the aluminium dissolution through a cathodic effect^{89, 99-101}. In a different context, Al anodizing is also affected by Cu-rich particles^{102, 103}. Indeed, it was demonstrated that the Cu species present in the IMCs and solid solution do not oxidize and they accumulate at the interface leading to the formation of a Cu-rich region/layer¹⁰³.

Nevertheless, there is still a lack of understanding and information with respect to the critical effect that these IMCs have on the LDH conversion coating formation. The current study does not provide enough data to provide relevant and definitive conclusions on what occurs at the level of IMCs. It is beyond the scope of the present research and will be reported elsewhere in the near future.

Table 2 summarizes the processes realized at each stage, and the observation made using the different characterization methods. It should be noted that the timeline shown in the table is specific to the current study.

Table 2. Description of the LDH growth according to the different characterization methods

Stage	Stage 0	Stage 1	Stage 2	Stage 3
Scheme				
XRD/ Kinetic analysis	<ul style="list-style-type: none"> - XRD Reflections associated with the AA2024 substrate. - No reflection associated with LDH 	<ul style="list-style-type: none"> - XRD Reflections associated with the AA2024 substrate. - No reflection associated with LDH - Detection of an amorphous halo associated with a signal from water and/or formation of an intermediate pseudo-boehmite layer 	<ul style="list-style-type: none"> - Appearance of first XRD reflections for LDH phase - First (003) reflection at $t = 21.6$ s and then (006) reflection after a few more seconds - Decrease of the intensity of the reflections associated with IMCs 	<ul style="list-style-type: none"> - Continuous increase of the LDH reflection intensity and decrease of the intensity of the reflections associated with the AA2024 IMC phases. - Increase of the size of the LDH flakes "L" (Scherrer calculations)
AFM/ SKPFM	<ul style="list-style-type: none"> - Observation of scattered IMCs and dispersoids on the VPD maps, which are more positive in potential than the Al matrix 	No measurement taken at this stage	<ul style="list-style-type: none"> - Complete coverage of the surface with LDH, including IMCs. - Increase of the overall VPD - Contribution of the Cu-rich IMC dealloying and redeposition on the overall VPD increase 	<ul style="list-style-type: none"> - Continuous increase of the VPD levels
OCP	- Decrease of the potential associated with the dissolution of the Al native oxide layer		- Increase of the potential till it reaches the first plateau	- Stable increase of the potential due to the thickening of the LDH layer
SEM	- Reference shows some scratches and no traces of LDH	No SEM image taken at this stage	<ul style="list-style-type: none"> - Appearance of the LDH flakes and coverage of the scratches at the interface - LDH film less compact 	<ul style="list-style-type: none"> - Change on the overall morphology of the LDH layer - LDH appears thicker and more compact.
Cross-section TEM/E DX	<p>→ TEM/EDX observation has been performed on the sample with completely formed LDH film.</p> <ul style="list-style-type: none"> - An intermediate layer is formed under the LDH layer - LDH flakes are mainly perpendicular to the surface but minor deviation from perpendicularity was observed in some regions. - There is a variation in element distribution along intermediate layer and LDH coating - A Cu-rich layer was observed at the interface of the AA2024 substrate and intermediate layer 			

Conclusions

The combination of *in-situ* and *ex-situ* methods was used to investigate the kinetics behind the mechanism of LDH conversion coating formation on an AA2024 substrate. The kinetic analysis of the data obtained by the *in-situ* synchrotron high-resolution XRD revealed that the LDH growth is a diffusion-controlled 2D-reaction with zero nucleation rate. The activities taking place at the interface were monitored by AFM/SKPFM together with OCP measurements, whereas the changes in morphology/structures were observed with TEM/EDX and SEM. Accordingly, the mechanism of LDH growth can be divided into three main stages:

- 1) The initiation stage consists of a fast conversion of the native oxide layer into a pseudo-boehmite (AlOOH) intermediate layer. Further depassivation of the Al substrate and dissolution promotes the growth of this intermediate layer.
- 2) The appearance of the first LDH flakes: following the increase of the local pH, the partial dissolution of the intermediate AlOOH layer occurs, liberation Al (OH)₄⁻ ions that react with Zn (OH)⁺ inducing an instantaneous nucleation and growth of the LDH flakes. This reaction is governed by a diffusion-controlled 2D reaction with a zero-nucleation rate.
- 3) Continuous thickening of LDH film leads to the formation of a dense LDH conversion coating. Although the overall formed LDH flakes exhibit a perpendicular orientation with respect to the interface, a minor disordered growth of the flakes and some voids can be observed between the LDH flakes.

This study also highlighted the crucial role played by Cu particles contained in the AA2024 on the overall mechanism of LDH growth. Indeed, IMC phases, specifically Cu-rich IMCs in the AA2024 alloy are known to play a key role in the initiation of conversion coating formation. Therefore, it is important to conduct a dedicated investigation of the influence of these IMC phases on the mechanism of LDH growth.

Supporting Information

Additional description and data supporting the different measurements; scheme of the *in-situ* XRD experimental set-up, Rietveld refined data, list of XRD peaks, additional AFM/SKPFM and kinetics data.

Acknowledgement

We acknowledge DESY (Hamburg, Germany), a member of the Helmholtz Association HGF, for the provision of experimental facilities. Parts of this research were carried out at PETRA III under the proposal number I-20170366. We would like to thank Dr. Sergey Volkov for his assistance in using the diffractometer in P08 high-resolution diffraction beamline.

We are also grateful to Dr. Petr Harcuba and Dr. Peter Minarik for help with TEM lamella preparation and Dr. Miroslav Cieslar for his assistance during TEM operation. We thank Gert Wiese for his help with obtaining the SEM micrographs.

ACB and MHI are grateful for the financial support of the German-Russian Interdisciplinary Science Center (G-RISC) in form of a travel grant (T-2018b-1 and T-2018a-3 respectively) that enabled them to perform a scientific exchange and complete this work. ACB additionally thanks the EFC young scientist for awarding the EUROCORN Young Scientist Grant 2017, financially supporting her research stay among the SURF group at Vrije Universiteit Brussel and accomplishing a part of the current study.

MS and MLZ are also thankful to I2B fond for financial support of this work in frame of MUFFin project as well as the ACTICOAT project in frame of Era.Net RUS Plus Call 2017 (Project 477).

KY acknowledges researcher grant (IF/01284/2015). A part of this work was developed within the scope of the project CICECO-Aveiro Institute of Materials, UIDB/50011/2020 & UIDP/50011/2020, financed by national funds through the Portuguese Foundation for Science and Technology/MCTES.

DD is grateful for the financial support of the Nanomaterials Centre for Advanced Applications (NANOCENT), grant number CZ.02.1.01/0.0/0.0/15_003/0000485 financed by ERDF.

AL gratefully acknowledges the funding of VLAIO for the RECYCAL 2 project with the number HBC.2017.0300.

Moreover, this work was the result of the participation of several other projects namely the European project MULTISURF and FUNCOAT in frame of the H2020-MSCA-RISE, grant agreement No 645676 and No 823942, respectively.

Declarations of interest: The authors declare no competing financial interest

Data availability: The raw/processed data required to reproduce these findings cannot be shared at this time as the data also forms part of an ongoing study.

References

- (1) Active Protective Coatings: New-Generation Coatings for Metals; Hughes, A.E, Mol, J.M.C., Zheludkevich, M.L., Buchheit, R.G, Eds. ; Springer Science+Business Media Dordrecht, 2016.
- (2) Twite, R.; Bierwagen, G.P. Review of Alternatives to Chromate for Corrosion Protection of Aluminum Aerospace Alloys. *Prog. Org. Coat.* **1998**, *33*, 91-100.
- (3) Xia, L.; McCreery, R.L. Chemistry of a Chromate Conversion Coating on Aluminum Alloy AA2024-T3 Probed by Vibrational Spectroscopy. *J. Electrochem. Soc.* **1998**, *145*, 3083-3089.
- (4) McGovern, W.R.; Schmutz, P.; Buchheit, R.G.; McCreery, R.L. Formation of Chromate Conversion Coatings on Al-Cu-Mg Intermetallic Compounds and Alloys. *J. Electrochem. Soc.* **2000**, *147*, 4494-4501.
- (5) Frankel, G.S.; McCreery, R.L. Inhibition of Al Alloy Corrosion by Chromates. *Electrochem. Soc. Interface* **2001**, *10*, 34-39.
- (6) Jaime Vasquez, M.; Halada, G.P.; Clayton, C.R.; Longtin, J.P. On the Nature of the Chromate Conversion Coating Formed on Intermetallic Constituents of AA2024-T3. *Surf. Interface Anal.* **2002**, *33*, 607-616.
- (7) Kendig, M.; Buchheit, R.L. Corrosion Inhibition of Aluminum and Aluminum Alloys by Soluble Chromates, Chromate Coatings, and Chromate-free Coatings. *Corrosion* **2003**, *59*, 379-400.

- (8) Hurley, B.L.; McCreery, R.L. Raman Spectroscopy of Monolayers Formed from Chromate Corrosion Inhibitor on Copper Surfaces. *J. Electrochem. Soc.* **2003**, *150*, B367-B373.
- (9) Bouali, A.C.; Serdechnova, M.; Blawert, C.; Tedim, J.; Ferreira, M.G.S.; Zheludkevich, M.L. Layered Double Hydroxides (LDHs) as Functional Materials for the Corrosion Protection of Aluminum Alloys: a Review. *Appl. Mater. Today* **2020**, *21*, 100857-1-100857-42.
- (10) O'Keefe, M.J.; Geng, S.; Joshi, S. Cerium-Based Conversion Coatings as Alternatives to Hex Chrome: Rare-Earth Compounds Provide Resistance Against Corrosion for Aluminum Alloys in Military Applications. *Met. Finish.* **2007**, *105*, 25-28.
- (11) Gharbi, O.; Thomas, S.; Smith, C.; Birbilis, N. Chromate Replacement: What Does the Future Hold?. *npj Mater Degrad.* **2018**, *2*, 1-8.
- (12) Shchukina, E.; Wang, H.; Shchukin, D.G. Nanocontainer-Based Self-Healing Coatings: Current Progress and Future Perspectives. *Chem. Commun.* **2019**, *55*, 3859-3867.
- (13) Qi, J.; Gao, L.; Liu, Y.; Liu, B.; Hashimoto, T.; Wang, Z.; Thompson, G.E. Chromate Formed in a Trivalent Chromium Conversion Coating on Aluminum. *J. Electrochem. Soc.* **2017**, *164*, C442-C449.
- (14) Ogle, K.; Tomandl, A.; Meddahi, N.; Wolpers, M. The Alkaline Stability of Phosphate Coatings I: ICP Atomic Emission Spectroelectrochemistry. *Corros. Sci.* **2004**, *46*, 979-995.
- (15) Tomandl, A.; Wolpers, M.; Ogle, K. The Alkaline Stability of Phosphate Coatings II: In-situ Raman Spectroscopy. *Corros. Sci.* **2004**, *46*, 997-1011.
- (16) Yi, A.; Li, W.; Du, J.; Mu, S. Preparation and Properties of Chrome-free Colored Ti/Zr Based Conversion Coating on Aluminum Alloy. *Appl. Surf. Sci.* **2012**, *258*, 5960-5964.

- (17) Carangelo, M.; Curioni, Acquesta, A., Monetta, T., Bellucci, F. Cerium-Based Sealing of Anodic Films on AA2024T3: Effect of Pore Morphology on Anticorrosion Performance. *J. Electrochem. Soc.* **2016**, *163*, C907-C916.
- (18) Milošev, I.; Frankel, G.S. Conversion Coatings Based on Zirconium and/or Titanium. *J. Electrochem. Soc.* **2018**, *165*, C127-C144.
- (19) Guo, Y.; Frankel, G.S. Active Corrosion Inhibition of AA2024-T3 by Trivalent Chrome Process Treatment. *Corrosion* **2012**, *68*, 045002-1-045002-10.
- (20) Ely, M.; Światowska, J.; Seyeux, A.; Zanna, A.; Marcus, P. Role of Post-treatment in Improved Corrosion Behavior of Trivalent Chromium Protection (TCP) Coating Deposited on Aluminum Alloy 2024-T3. *J. Electrochem. Soc.* **2017**, *164*, C276-C284.
- (21) Sankara Narayanan, T. Surface Pretreatment by Phosphate Conversion Coatings-A Review. *Rev. Adv. Mater. Sci.* **2005**, *9*, 130-177.
- (22) Yoganandan, G.; Premkumar, K.P.; Balaraju, J. Evaluation of Corrosion Resistance and Self-Healing Behavior of Zirconium–Cerium Conversion Coating Developed on AA2024 Alloy. *Surf. Coat. Technol.* **2015**, *270*, 249-258.
- (23) Fahrenholtz, W.G.; O'Keefe, M.J.; Zhou, H.; Grant, J.T. Characterization of Cerium-Based Conversion Coatings for Corrosion Protection of Aluminum Alloys. *Surf. Coat. Technol.* **2002**, *155*, 208-213.
- (24) Hughes, A.E.; Taylor, R.; Hinton, B.R.W. Chromate Conversion Coatings on 2024 Al Alloy. *Surf. Interface Anal.* **1997**, *25*, 223-234.
- (25) Kendig, M.; Davenport, A.; Isaacs, H. The Mechanism of Corrosion Inhibition by Chromate Conversion Coatings from X-ray Absorption Near Edge Spectroscopy (XANES). *Corros. Sci.* **1993**, *34*, 41-49.
- (26) Kolics, A.; Besing, A.S.; Baradlai, P.; Wieckowski, A. Cerium Deposition on Aluminum Alloy 2024-T3 in Acidic NaCl Solutions. *J. Electrochem. Soc.* **2003**, *150*, B512-B516.

- (27) Bethencourt, M.; Botana, F.J.; Cano, M.J.; Marcos, M. Advanced Generation of Green Conversion Coatings for Aluminium Alloys. *Appl. Surf. Sci.* **2004**, *238*, 278-281.
- (28) Conde, A.; Arenas, M.A.; De Frutos, A.; De Damborenea, J. Effective Corrosion Protection of 8090 Alloy by Cerium Conversion Coatings. *Electrochim. Acta* **2008**, *53*, 7760-7768.
- (29) Cerezo, J.; Vandendael, I.; Posner, R.; De Wit, J.H.W.; Mol, J.M.C.; Terryn, H. The Effect of Surface Pre-conditioning Treatments on the Local Composition of Zr-based Conversion Coatings Formed on Aluminium Alloys. *Appl. Surf. Sci.* **2016**, *366*, 339-347.
- (30) Cerezo, J.; Vandendael, I.; Posner, R.; Lill, K.; De Wit, J.H.W.; Mol, J.M.C.; Terryn, H. Initiation and Growth of Modified Zr-Based Conversion Coatings on Multi-metal Surfaces. *Surf. Coat. Technol.* **2013**, *236*, 284-289.
- (31) Becker, M. Chromate-Free Chemical Conversion Coatings for Aluminum Alloys, *Corros. Rev.* **2019**, *37*, 321-342.
- (32) Tabish, M.; Yasin, G.; Anjum, M.J.; Malik, M.U.; Zhao, J.; Yang, Q.; Manzoor, S.; Murtaza, H.; Khan, W.G. Reviewing the Current Status of Layered Double Hydroxide-Based Smart Nanocontainers for Corrosion Inhibiting Applications. *J. Mater. Res. Technol.* **2021**, *10*, 390-421.
- (33) Evans, D.G.; Slade, R.C.T. In *Layered Double Hydroxides. Structure and Bonding*; Duan, X., Evans, D.G., Eds.; Springer: Berlin, Heidelberg, 2006, Vol. 119, pp 1-87.
- (34) Leggat, R.B.; Zhang, W.; Buchheit, R.G.; Taylor, S.R. Performance of Hydrotalcite Conversion Treatments on AA2024-T3 when Used in a Coating System. *Corrosion* **2002**, *58*, 322-328.
- (35) Yasakau, K.A.; Kuznetsova, A.; Kallip, S.; Starykevich, M.; Tedim, J.; Ferreira, M.G.S.; Zheludkevich, M.L. A Novel Bilayer System Comprising LDH Conversion

- Layer and Sol-Gel Coating for Active Corrosion Protection of AA2024. *Corros. Sci.* **2018**, *143*, 299-313.
- (36) Serdechnova, M.; Ivanov, V.L.; Domingues, M.R.M.; Evtuguin, D.V.; Ferreira, M.G.S.; Zheludkevich, M.L. Photodegradation of 2-Mercaptobenzothiazole and 1, 2, 3-Benzotriazole Corrosion Inhibitors in Aqueous Solutions and Organic Solvents. *Phys. Chem. Chem. Phys.* **2014**, *16*, 25152-25160.
- (37) Zheludkevich, M.L.; Poznyak, S.K.; Rodrigues, L.M.; Raps, D.; Hack, T.; Dick, L.F.; Nunes, T.; Ferreira, M.G.S. Active Protection Coatings with Layered Double Hydroxide Nanocontainers of Corrosion Inhibitor. *Corros. Sci.* **2010**, *52*, 602-611.
- (38) Zhang, F. ; Zhang, C.L.; Liang, S.; Zeng, R.C.; Liu, Z.G.; Cui, H.Z. Corrosion of In-situ Grown MgAl-LDH Coating on Aluminum Alloy. *T. Nonferr. Metal Soc.* **2015**, *25*, 3498-3504.
- (39) Tedim, J.; Zheludkevich, M.L.; Salak, A.N.; Lisenkov, A.; Ferreira, M.G.S. Nanostructured LDH-Container Layer with Active Protection Functionality. *J. Mater. Chem.* **2011**, *21*, 15464-15470.
- (40) Zhang, W.; Buchheit, R.G. Hydrotalcite Coating Formation on Al-Cu-Mg Alloys from Oxidizing Bath Chemistries. *Corrosion* **2002**, *58*, 591-600.
- (41) Visser, P.; Meeusen, M.; Gonzalez-Garcia, Y.; Terryn, H.; Mol, J.M.C. Electrochemical Evaluation of Corrosion Inhibiting Layers Formed in a Defect from Lithium-Leaching Organic Coatings. *J. Electrochem. Soc.* **2017**, *164*, C396-C406.
- (42) Buchheit, R.G.; Bode, M.; Stoner, G. Corrosion-Resistant, Chromate-Free Talc Coatings for Aluminum. *Corrosion* **1994**, *50*, 205-214.
- (43) Wang, Y.; Zhang, Y.; Zhou, B.; Li, C.; Gao, F.; Wang, X.; Liang, D.; Wei, Y. In-situ Observation of the Growth Behavior of ZnAl Layered Double Hydroxide Film Using EQCM. *Mater. Des.* **2019**, *180*, 107952-1-107952-9.

- (44) Buchheit, R.G.; Grant, R.P.; Hlava, P.F.; McKenzie, B.; Zender, G.L. Local Dissolution Phenomena Associated with S-Phase (Al₂CuMg) Particles in Aluminum Alloy 2024-T3. *J. Electrochem. Soc.* **1997**, *144*, 2621-2628.
- (45) Visser, P.; Gonzalez-Garcia, Y.; Mol, J.M.C.; Terryn, H. Mechanism of Passive Layer Formation on AA2024-T3 from Alkaline Lithium Carbonate Solutions in the Presence of Sodium Chloride. *J. Electrochem. Soc.* **2018**, *165*, C60-C70.
- (46) Tedim, J.; Zheludkevich, M.L.; Bastos, A.C.; Salak, A.N.; Lisenkov, A.D.; Ferreira, M.G.S. Influence of Preparation Conditions of Layered Double Hydroxide Conversion Films on Corrosion Protection. *Electrochem. Acta* **2014**, *117*, 164-171.
- (47) Kuznetsov, B.; Serdechnova, M.; Tedim, J.; Starykevich, M.; Kallip, S.; Oliveira, M.P.; Hack, T.; Nixon, S.; Zheludkevich, M.L. Sealing of Tartaric Sulfuric (TSA) Anodized AA2024 with Nanostructured LDH Layers. *Rsc Adv.* **2016**, *6*, 13942-13952.
- (48) Seeck, O.H.; Deiter, C.; Pflaum, K.; Bertam, F.; Beerlink, A.; Franz, H.; Horbach, J.; Schulte-Schrepping, H.; Murphy, B.M.; Greve, M.; Magnussen, O. The High-Resolution Diffraction Beamline P08 at PETRA III. *J. Synchrotron Radiat.* **2012**, *19*, 30-38.
- (49) Bouali, A.C.; Iuzviuk, M.H.; Serdechnova, M.; Yasakau, K.A.; Wieland, D.C.F.; Dovzhenko, G.; Maltanava, H.; Zobkalo, I.A.; Ferreira, M.G.S.; Zheludkevich, M.L. Zn-Al LDH Growth on AA2024 and Zinc and their Intercalation with Chloride: Comparison of Crystal Structure and Kinetics. *Appl. Surf. Sci.* **2020**, *501*, 144027-14036.
- (50) Rohwerder, M.; Turcu, F. High-Resolution Kelvin Probe Microscopy in Corrosion Science: Scanning Kelvin Probe Force Microscopy (SKPFM) Versus Classical Scanning Kelvin Probe (SKP). *Electrochim. Acta* **2007**, *53*, 290-299.
- (51) Yasakau, K.A.; Höche, D.; Lamaka, S.L.; Ferreira, M.G.S.; Zheludkevich, M.L. Kelvin Microprobe Analytics on Iron-Enriched Corroded Magnesium Surface. *Corrosion* **2017**, *73*, 583-595.

- (52) Cook, A.B.; Barrett, Z.; Lyon, S.B.; McMurray, H.N.; Walton, J.; Williams, G. Calibration of the Scanning Kelvin Probe Force Microscope Under Controlled Environmental Conditions. *Electrochim. Acta* **2012**, *66*, 100-105.
- (53) Hausbrand, R.; Stratmann, M.; Rohwerder, M. The Physical Meaning of Electrode Potentials at Metal Surfaces and Polymer/Metal Interfaces: Consequences for Delamination. *J. Electrochem. Soc.* **2008**, *155*, C369-C379.
- (54) Marappa, S.; Radha, S.; Kamath, P.V. Nitrate-Intercalated Layered Double Hydroxides—Structure Model, Order, and Disorder. *Eur. J. Inorg. Chem.* **2013**, *2013*, 2122-2128.
- (55) Yasakau, K.A.; Zheludkevich, M.L.; Lamaka, S.V.; Ferreira, M.G.S. Mechanism of Corrosion Inhibition of AA2024 by Rare-Earth Compounds. *J. Phys. Chem B* **2006**, *110*, 5515-5528.
- (56) Schmutz, P.; Frankel, G.S. Characterization of AA2024-T3 by Scanning Kelvin Probe Force Microscopy. *J. Electrochem. Soc.* **1998**, *145*, 2285-2295.
- (57) Lunder, O.; Walmsley, J.C.; Mack, P.; Nisancioglu, K. Formation and Characterisation of a Chromate Conversion Coating on AA6060 Aluminium. *Corros. Sci.* **2005**, *47*, 1604-1624.
- (58) Shirvani, K.; Mastali, S. Effect of Grain Refinement and Immersion Time on Morphology, Topography and Corrosion Resistance of CCC-Coated 7075 Al Alloy. *J. Electrochem. Soc.* **2011**, *159*, C74-C79.
- (59) Grundmeier, G.; Stratmann, M. Influence of Oxygen and Argon Plasma Treatments on the Chemical Structure and Redox State of Oxide Covered Iron. *Appl. Surf. Sci.* **1999**, *141*, 43-56.

- (60) Yasakau, K.A.; Salak, A.N.; Zheludkevich, M.L.; Ferreira, M.G.S. Volta Potential of Oxidized Aluminum Studied by Scanning Kelvin Probe Force Microscopy. *J. Phys. Chem. C* **2010**, *114*, 8474-8484.
- (61) Lacroix, L.; Ressler, L.; Blanc, C.; Mankowski, G. Combination of AFM, SKPFM, and SIMS to Study the Corrosion Behavior of S-Phase Particles in AA2024-T351. *J. Electrochem. Soc.* **2008**, *155*, C131-C137.
- (62) Cornette, P.; Zanna, S.; Seyeux, A.; Costa, D.; Marcus, P. The Native Oxide Film on a Model Aluminium-Copper Alloy Studied by XPS and ToF-SIMS. *Corros. Sci.* **2020**, *174*, 108837.
- (63) Tao, J. Surface Composition and Corrosion Behavior of an Al-Cu Alloy. Ph.D. Dissertation, Pierre et Marie Curie - Paris VI, Paris, 2016.
- (64) Hashimoto, T.; Zhang, X.; Zhou, X.; Skeldon, P.; Haigh, S.J.; Thompson, G.E. Investigation of Dealloying of S-Phase (Al_2CuMg) in AA 2024-T3 Aluminium Alloy Using High Resolution 2D and 3D Electron Imaging. *Corros. Sci.* **2016**, *103*, 157-164.
- (65) Serdechnova, M.; Salak, A.N.; Barbosa, F.S.; Vieira, D.E.; Tedim, J.; Zheludkevich, M.L.; Ferreira, M.G.S. Interlayer Intercalation and Arrangement of 2-Mercaptobenzothiazolate and 1, 2, 3-Benzotriazole Anions in Layered Double Hydroxides: In situ X-ray Diffraction Study. *J. Solid State Chem.* **2016**, *233*, 158-165.
- (66) Mikhailau, A.; Maltanova, H.; Poznyak, S.K.; Salak, A.N.; Zheludkevich, M.L.; Yasakau, K.A.; Ferreira, M.G.S. One-Step Synthesis and Growth Mechanism of Nitrate Intercalated ZnAl LDH Conversion Coatings on Zinc. *Chem. Commun.* **2019**, *55*, 6878-6881.
- (67) Avrami, M. Kinetics of Phase change. I General Theory. *J. Phys. Chem.* **1939**, *7*, 1103-1112.
- (68) Avrami, M. Kinetics of Phase Change. II Transformation-Time Relations for Random Distribution of Nuclei. *J. Chem. Phys.* **1940**, *8*, 212-224.

- (69) Avrami, M. Granulation, Phase Change, and Microstructure Kinetics of Phase Change. III. *J. Phys. Chem.* **1941**, *9*, 177-184.
- (70) Zhou, Y.; Antonova, E.; Bensch, W.; Patzke, G.R. In situ X-ray Diffraction Study of the Hydrothermal Crystallization of Hierarchical Bi₂WO₆ Nanostructures. *Nanoscale* **2010**, *2*, 2412-2417.
- (71) Williams G.R.; Khan A.I.; O'Hare D. In Layered Double Hydroxides. Structure and Bonding; Duan, X., Evans, D.G., Eds.; Springer: Berlin, Heidelberg, 2006, Vol. 119, pp 161-192.
- (72) Iuzviuk, M.H.; Bouali, A.C.; Serdechnova, M.; Yasakau, K.A.; Wieland, D.C.F.; Dovzhenko, G.; Mikhailau, A.; Blawert, C.; Zobkaloa, I.A.; Ferreira, M.G.S.; Zheludkevich, M.L. In-situ Kinetics Studies of Zn-Al LDH Intercalation with Corrosion Related Species. *Phys. Chem. Chem. Phys.* **2020**, *22*, 17574-17586.
- (73) Hancock, J.; Sharp, J. Method of Comparing Solid-State Kinetic Data and its Application to the Decomposition of Kaolinite, Brucite, and BaCO₃. *J. Am. Ceram. Soc.* **1972**, *55*, 74-77.
- (74) Hulbert, S. Models For Solid-State Reactions in Powdered Compacts: A Review. *J. Brit. Ceram. Soc.* **1969**, *6*, 11-20.
- (75) Chen, M.; Zhu, R.; Zhu, J.; He, H. Temperature-Dependent Structure and Dynamics of Water Intercalated in Layered Double Hydroxides with Different Hydration States. *J. Phys. Chem. C* **2017**, *121*, 23752-23762.
- (76) Nieto-Malagón, G.; Cautli, C.; Ireta, J. Interlaminar Anionic Transport in Layered Double Hydroxides: Estimation of Diffusion Coefficients. *J. Phys. Chem. C* **2018**, *122*, 171-176.

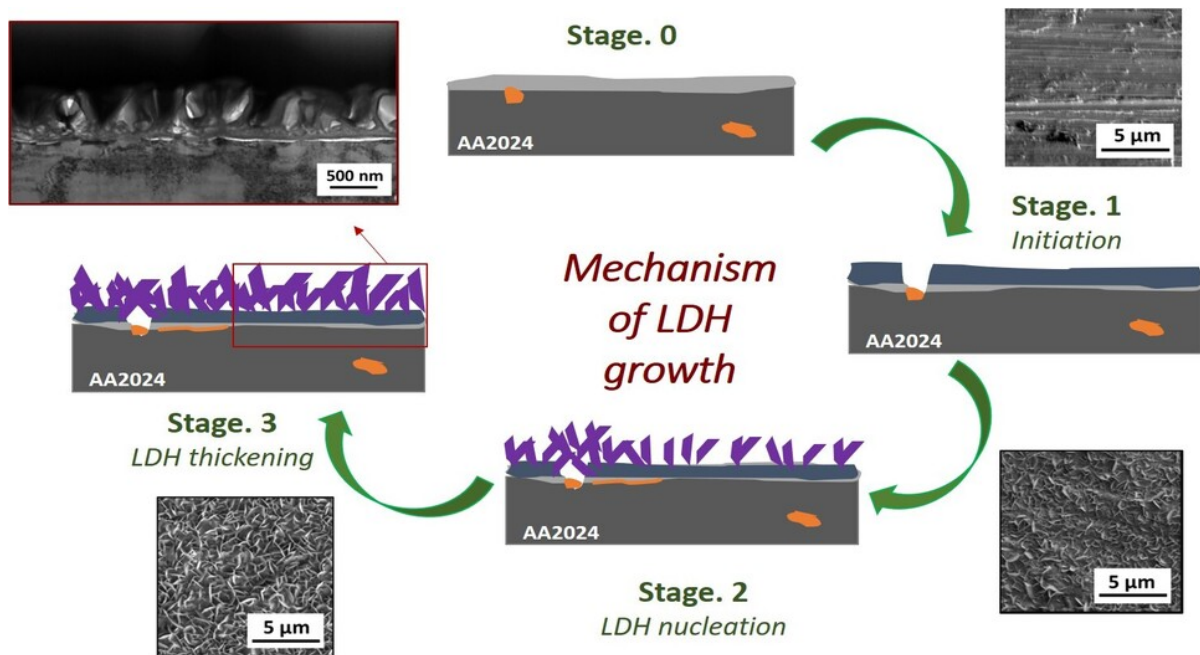
- (77) Bouali, A.C.; Iuzviuk, M.H.; Serdechnova, M.; Yasakau, K.A.; Wieland, D.C.F.; Dovzhenko, G.; Maltnava, H.; Zobkalo, I.A.; Ferreira, M.G.S.; Zheludkevich, M.L. Zn-Al LDH Growth on AA2024 and Zinc and their Intercalation with Chloride: Comparison of Crystal Structure and Kinetics. *Appl. Surf. Sci.* **2020**, *501*, 144027-1-144027-10.
- (78) Scherrer, P. Determination of the Size and Internal Structure of Colloidal Particles Using X-rays, *Nachr. Ges. Wiss. Göttingen* **1918**, *2*, 98-100.
- (79) Lü, Z.; Zhang, F.; Lei, X.; Yang, L.; Xu, S.; Duan, X. In situ Growth of Layered Double Hydroxide Films on Anodic Aluminum Oxide/Aluminum and its Catalytic Feature in Aldol Condensation of Acetone. *Chem. Eng. Sci.* **2008**, *63*, 4055-4062.
- (80) Hoshino, K.; Furuya, S.; Buchheit, R.G. Effect of Solution pH on Layered Double Hydroxide Formation on Electrogalvanized Steel Sheets. *J. Mater. Eng. Perform.* **2019**, *28*, 2237-2244.
- (81) Visser, P.; Gonzalez-Garcia, Y.; Mol, J.M.C.; Terryn, H. Mechanism of Passive Layer Formation on AA2024-T3 from Alkaline Lithium Carbonate Solutions in the Presence of Sodium Chloride. *J. Electrochem. Soc.* **2018**, *165*, C60-C70.
- (82) Bunker, B.C.; Nelson, G.C.; Zavadil, K.R.; Barbour, J.C.; Wall, F.D.; Sullivan, J.P.; Windisch, C.F.; Engelhardt, M.H.; Baer, D.R. Hydration of Passive Oxide Films on Aluminum. *J. Phys. Chem. B* **2002**, *106*, 4705-4713.
- (83) Deng, Z.Y.; Ferreira, J.M.F.; Tanaka, Y.; Ye, J. Physicochemical Mechanism for the Continuous Reaction of γ -Al₂O₃-Modified Aluminum Powder with Water. *J. Am. Ceram. Soc.* **2007**, *90*, 1521-1526.
- (84) Serdechnova, M.; Mohedano, M.; Kuznetsov, B.; Mendis, C.L.; Strykevich, M.; Karpushenkov, S.; Tedim, J.; Ferreira, M.G.S.; Blawert, C.; Zheludkevich, M.L. PEO coatings with active protection based on in-situ formed LDH-nanocontainers, *J. Electrochem. Soc.* **2016**, *164*, C36-C45.

- (85) Buchheit, R.G.; Martinez, M.; Montes, L. Evidence for Cu Ion Formation by Dissolution and Dealloying the Al₂CuMg Intermetallic Compound in Rotating Ring-Disk Collection Experiments. *J. Electrochem. Soc.* **2000**, *147*, 119-124.
- (86) Vukmirovic, M.; Dimitrov, N.; Sieradzki, K. Dealloying and Corrosion of Al Alloy 2024-T3. *J. Electrochem. Soc.* **2002**, *149*, B428-B439.
- (87) Kosari, A.; Zandbergen, H.; Tichelaar, F.; Visser, P.; Taheri, P.; Terryn, H.; Mol, J.M.C. In-situ Nanoscopic Observations of Dealloying-Driven Local Corrosion from Surface Initiation to In-Depth Propagation. *Corros. Sci.* **2020**, *177*, 108912-1-108912-12.
- (88) Kosari, A.; Tichelaar, F.; Visser, P.; Zandbergen, H.; Terryn, H.; Mol, J.M.C. Dealloying-Driven Local Corrosion by Intermetallic Constituent Particles and Dispersoids in Aerospace Aluminium Alloys. *Corros. Sci.* **2020**, *177*, 108947-1-108947-11.
- (89) Mokaddem, M.; Volovitch, P.; Rechou, E.; Oltra, R.; Ogle, K. The Anodic and Cathodic Dissolution of Al and Al–Cu–Mg Alloy. *Electrochim. Acta* **2010**, *55*, 3779-3786.
- (90) Habashi, F. Kinetics and Mechanism of Copper Dissolution in Aqueous Ammonia, *Berichte der Bunsengesellschaft für physikalische Chemie (Früher Zeitschrift für Elektrochemie)*. *J. Phys. Chem. Chem. Phys.* **1963**, *67*, 402-406.
- (91) Trevani, L.N.; Roberts, J.C.; Tremaine, P.R. Copper (II)–Ammonia Complexation Equilibria in Aqueous Solutions at Temperatures from 30 to 250° C by Visible Spectroscopy. *J. solution chem.* **2001**, *30*, 585-622.
- (92) Johnson, A.R.; McQueen, T.M.; Rodolfa, K.T. Species Distribution Diagrams in the Copper-Ammonia System: An Updated and Expanded Demonstration Illustrating Complex Equilibria. *J. Chem. Educ.* **2005**, *82*, 408-414.
- (93) Radmehr, V.; Koleini, S.M.J.; Khalesi, M.R.; Tavakoli, M.R. *In XXVI International Mineral Processing Congress (IMPC)*, Proceedings, New Delhi, India, 24-28 September, 2012, pp. 02512-02523

- (94) Konishi, H.; Bitoh, H.; Ono, H.; Oishi, T.; Koyama, K.; Tanaka, M. Behavior of Copper Dissolution in an Ammonia Solution Containing Ammonium Chloride or Sulfate, *JSEM*. **2014**, *14*, 205-209.
- (95) Luo, Q.; Mackay, R.A.; Babu, S.V. Copper Dissolution in Aqueous Ammonia-Containing Media During Chemical Mechanical Polishing. *Chem. Mater.* **1997**, *9*, 2101-2106.
- (96) Qi, J.T.; Hashimoto, T.; Walton, J.R.; Zhou, X.; Skeldon, P.; Thompson, G.E. Trivalent Chromium Conversion Coating Formation on Aluminium. *Surf. Coat. Technol.* **2015**, *280*, 317-329.
- (97) Akhtar, A.S.; Wong, K.; Mitchell, K.A.R. The Effect of pH and Role of Ni²⁺ in Zinc Phosphating of 2024-Al Alloy: Part I: Macroscopic Studies with XPS and SEM. *Appl. Surf. Sci.* **2006**, *253*, 493-501.
- (98) Akhtar, A.S.; Susac, D.; Wong, P.C.; Mitchell, K.A.R. The Effect of pH and Role of Ni²⁺ in Zinc Phosphating of 2024-Al Alloy: Part II: Microscopic Studies with SEM and SAM. *Appl. Surf. Sci.* **2006**, *253*, 502-509.
- (99) Mokaddem, M.; Volovitch, P.; Rechou, E.; Oltra, R.; Ogle, K. The Anodic and Cathodic Dissolution of Al and Al–Cu–Mg Alloy. *Electrochim. Acta* **2010**, *55*, 3779-3786.
100. Serdechnova, M.; Volovitch, P.; Brisset, F.; Ogle, K. On the Cathodic Dissolution of Al and Al Alloys. *Electrochim. Acta* **2014**, *124*, 9-16.
101. Boag, A.; Hughes, A.E.; Glenn, A.M.; Muster, T.H.; McCulloch, D. Corrosion of AA2024-T3 Part I: Localised Corrosion of Isolated IM Particles. *Corros. Sci.* **2011**, *53*, 17-26.

102. Curioni, M.; De Miera, M.S.; Skeldon, P.; Thompson, G.E.; Ferguson, J. Macroscopic and Local Filming Behavior of AA2024 T3 Aluminum Alloy During Anodizing in Sulfuric Acid Electrolyte. *J. Electrochem. Soc.* **2008**, *155*, C387-C395.
103. Martínez-Viademonte, M.P.; Abrahami, S.T.; Hack, T.; Burchardt, M.; Terryn, H. A Review on Anodizing of Aerospace Aluminum Alloys for Corrosion Protection. *Coatings* **2020**, *10*, 1109-1-1109-30.

Table of content graphic



The LDH growth is governed by a 2D diffusion-controlled reaction with a zero-nucleation rate. Moreover, a formation of a pseudo-boehmite intermediate layer together with a Cu-rich layer were observed prior to the appearance of the first LDH flakes.